Efficient laser-induced 6 - 8 keV x-ray production from iron oxide aerogel and foil-lined cavity targets

F. Perez, J. J. Kay, R. Patterson, J. Kane, B. Villette, F. Girard, C. Reverdin, M. May, J. Emig, C. Sorce, J. Colvin, S. Gammon, J. Jaquez, J. Satcher, K. B. Fournier

Disclaimer

This document was prepared as an account of work sponsored by an agency of the United States government. Neither the United States government nor Lawrence Livermore National Security, LLC, nor any of their employees makes any warranty, expressed or implied, or assumes any legal liability or responsibility for the accuracy, completeness, or usefulness of any information, apparatus, product, or process disclosed, or represents that its use would not infringe privately owned rights. Reference herein to any specific commercial product, process, or service by trade name, trademark, manufacturer, or otherwise does not necessarily constitute or imply its endorsement, recommendation, or favoring by the United States government or Lawrence Livermore National Security, LLC. The views and opinions of authors expressed herein do not necessarily state or reflect those of the United States government or Lawrence Livermore National Security, LLC, and shall not be used for advertising or product endorsement purposes.

Efficient laser-induced 6 - 8 keV x-ray production from iron oxide aerogel and foil-lined cavity targets

F. Pérez,[1, a)] J. J. Kay,[1, b)] J. R. Patterson,[1] J. Kane,[1] B. Villette,[2] F. Girard,[2] C. Reverdin,[2] M. May,[1] J. Emig,[1] C. Sorce,[1, 3] J. Colvin,[1] S. Gammon,[1] J. Jaquez,[4] J. H. Satcher, Jr,[1] and K. B. Fournier[1]

[1)] *Lawrence Livermore National Laboratory, 7000 East Avenue, Livermore, California 94550*

[2)] *CEA DAM DIF, F-91297 Arpajon, France*

[3)] *University of Rochester - Laboratory for Laser Energetics, 250 E. River Rd, Rochester, NY 14623-1299*

[4)] *General Atomics, San Diego, CA 92121*

The performance of new iron-based laser-driven x-ray sources has been tested at the OMEGA laser facility for production of x rays in the $6.5 - 8.5$ keV range. Two types of targets were experimentally investigated: low-density iron oxide aerogels (density $6 - 16$ mg/cm^3) and stainless steel foil-lined cavity targets (steel thickness $1 - 5$ μm). The targets were irradiated by 40 beams of the OMEGA laser (500 J/beam, 1 ns pulse, wavelength 351 nm). All targets showed good coupling with the laser, with $< 5\%$ of the incident laser light backscattered by the resulting plasma in all cases (typically $< 2.5\%$). The aerogel targets produced $T_e = 2$ to 3 keV, $n_e = 0.12 - 0.2$ critical density plasmas yielding a $40 - 60\%$ laser-to-x-ray total conversion efficiency ($1.2 - 3\%$ in the Fe K-shell range). The foil cavity targets produced $T_e \sim 2$ keV, $n_e \sim 0.15$ critical density plasmas yielding a $60 - 75\%$ conversion efficiency ($1.6 - 2.2\%$ in the Fe K-shell range). Time-resolved images illustrate that the volumetric heating of low-density aerogels allow them to emit a higher K-shell x-ray yield even though they contain fewer Fe atoms. However, their challenging fabrication process leads to a larger shot-to-shot variation than cavity targets.

PACS numbers: 52.38.Ph, 52.50.Jm

I. INTRODUCTION

Bright multi-keV x-ray sources are keenly needed in Inertial Confinement Fusion (ICF) and High Energy Density (HED) research. For example, they are required for radiography in ICF implosions, laser-driven shock experiments, and laboratory astrophysics experiments. Laser-irradiated foils have typically been employed as x-ray sources in these applications. However, the high-density plasma generated during ablation of solid planar targets prevents the laser from fully penetrating the target material, limiting the laser-to-K-shell-x-ray conversion efficiency (CE) to a fraction of a percent[1]. New approaches are required to develop brighter x-ray sources. Low-density targets, which allow full volumetric heating of the emitting material by the laser, is one of them. Our group has demonstrated CE's for x-ray energies > 2 keV from 1 to 10 % using pre-exploded foils[2,3], metal-doped aerogels[4,5], metal oxide nanofiber[6], and gas-filled[7,8] targets. Shaped targets, which confine, collect and allow further heating of low-density plasmas ablated from solid target walls, can also substantially increase x-ray conversion efficiency; foil-lined holhraums and halfraums demonstrated CEs of up to 7%[9,10].

In this paper we present the results of two campaigns to characterize new iron-based x-ray sources, and in particular their emission in the iron K-shell band ($6.5 - 8.5$ keV). This feature completes the previous works cited above, mainly focused on Ti (4.7 keV) and Ge (10.3 keV) targets, by introducing an intermediate x-ray energy. The present work is also the first demonstration of an underdense plasma radiation source made from a pure metal-oxide aerogel: previous studies were based on metal dopants and sometimes included chemical substitution to increase the metal concentration[5]. These metal-oxide aerogels have proven to be more difficult to fabricate than silica aerogels with dopants, but their quality will improve as this technique is further explored. The iron oxide aerogel targets (aerogel density $6 - 16$ mg/cm^3) are designed to produce plasmas with nominal densities that are $20 - 50\%$ of the critical density n_c for propagation of 351 nm (3ω) laser light. The lower end of this range of densities may allow volumetric heating of the foam by the laser and result in high x-ray conversion efficiency. Note that a lower aerogel density means lower electron density, which also implies a lower x-ray yield[11]. As a consequence, the foam density for maximum CE is a careful tradeoff between these two competing effects. Because of the complexity of x-ray generation in hot and dense plasmas, simulations are rarely precise enough to determine which one is the most significant. Thus, the present article is based on experimental results showing more efficient aerogels at lower densities.

In addition to these aerogel targets, we tested stainless steel foil-lined cavity targets. They consist of thin epoxy tubes lined with $1 - 5$ μm of stainless steel, and are designed to confine plasma ablated from the target walls to prevent cooling and allow further heating by the laser. Both types of targets, which were designed and optimized using the LASNEX radiation-hydrodynamics code[12], performed as expected or better, and will be used in upcom-
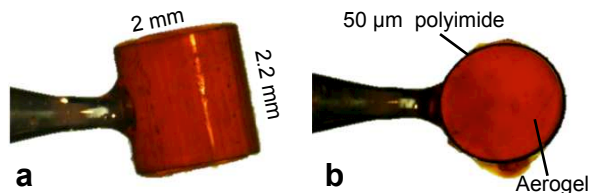
FIG. 1. (Color online) Photographs of an iron-oxide-aerogel target: (a) side view, (b) end view.

ing experiments on the National Ignition Facility[13].

Section II describes the target, laser and diagnostic configurations used in the experiments. Lasnex simulations are discussed in section III, showing the expected hydrodynamic behavior of each type of target. Measured data are presented in section IV, with comparisons to the relevant simulations. Section V concludes on the efficiency of each target type, and compares the present results to those from previous similar experiments.

II. EXPERIMENTAL SETUP

A. Targets

The aerogel targets (see Fig. 1) consist of polyimide tubes ($C_{22}H_{10}N_2O_5$, 50 μm wall thickness, 2000 μm inner diameter, 2200 μm length) filled with ultra-low-density iron oxide aerogel material. The aerogels are synthesized directly in the polyimide tubes by reaction of 3,3-dimethyloxetane with $FeCl_3 \cdot 6H_2O$ in an ethanol/water solution, followed by extraction of the solvent using supercritical CO_2[14]. The chemical composition of the resulting aerogels is $FeO_2HCl_{0.38}$. Aerogels were produced with densities of 3, 6.5, 12.5, and 16 mg/cm^3. Note that the lowest density aerogels are not included in the following discussion because their quality appeared too low to extract any useful data. According to lasnex simulations, the aerogel targets are expected to produce plasmas of electron density $n_e/n_c \sim 0.2 - 0.7$ and temperature $T_e \sim 2 - 3$ keV.

The stainless steel foil targets (see Fig. 2) consist of epoxy tubes (bisphenol-A-based epoxy resin, 50 μm wall thickness, 2000 μm inner diameter, 2200 μm length) lined with a $1 - 5$ μm thick layer of stainless steel 304. The atomic composition of the stainless steel foil is 70% Fe, 17% Cr, 9% Ni, 1.5% Mn, 1.5% Si, and 1% Mo. The targets are produced by sputter-coating an Al rod with stainless steel. An epoxy layer is then applied on top of the steel, and the Al is etched away using NaOH. These foil cavity targets are expected to produce plasmas with $n_e/n_c \sim 0.1 - 0.3$ and temperature $T_e \sim 1.5 - 2.5$ keV according to lasnex simulations.
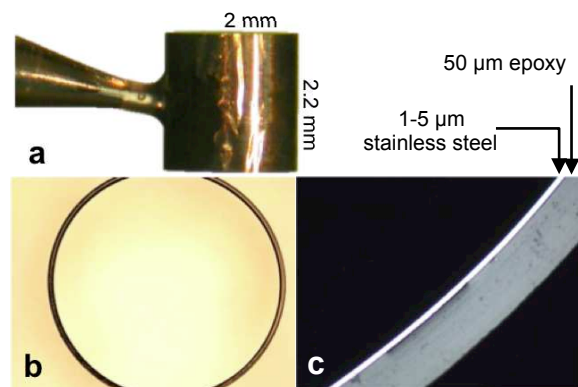

FIG. 2. (Color online) Photographs of a steel-lined cavity target: (a) side view, (b) end view, (c) inset of end view.

B. Lasers

All targets were irradiated by 40 beams of the omega laser (Laboratory for Laser Energetics, Rochester, NY)[15], arranged into three cones in a holhraum configuration along the P5-P8 axis of the target chamber for the first campaign, and along the P6-P7 axis for the second campaign. Fig. 3 illustrates the position of each cone: cone 1 and 2 contain 10 beams each, and cone 3 contains 20 beams. Each beam delivered $\sim$ 500 J to the target in a 1 ns square pulse (SG1018 pulse shape), for a total of 20 kJ on target at the wavelength 351 nm. The beams are timed to reach the faces/entrance holes of the target
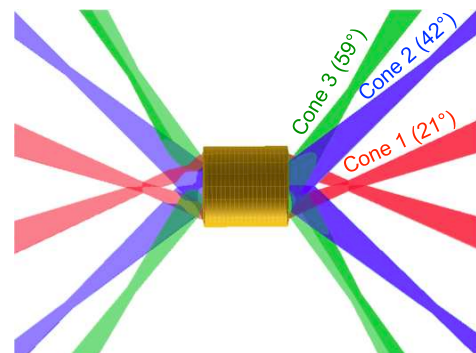

FIG. 3. (Color online) Schematic of the target and laser beams showing the three cones orientations.
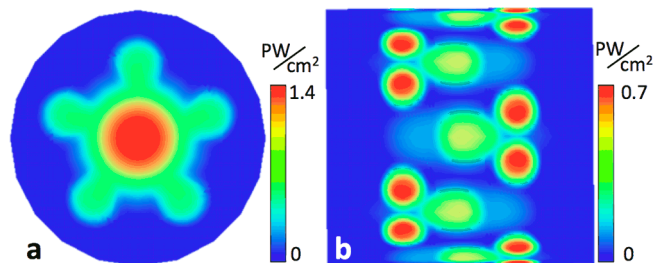

FIG. 4. (Color online) Laser irradiation patterns on (a) the end of aerogel targets and (b) the inside wall of cavity targets.

in coincidence. All beams are equipped with E-IDI-300[16] phase plate optics, which produce spatially smooth beam profiles (212 μm × 288 μm elliptical spot at best focus). The irradiation pattern on the face of the aerogel targets, or on the inside wall of cavity targets is plotted on Fig. 4. Details regarding the OMEGA laser, the target chamber, and each diagnostic instrument can be found in the National Laser User Facility User's Guide[17].

C. Time-integrated x-ray spectrometers

These experiments employed two time-integrated bent-crystal x-ray spectrometers: HENWAY[18] and XCCS. The HENWAY was equipped with two pentaerythritol (PET) crystals mounted to observe x-ray emission in the $5 - 13$ keV range, which spans all Fe K-shell emission lines $(6.5 - 8.5$ keV). The resolution of the spectrometer is approximately $30 - 50$ eV over the $6.5 - 8.5$ keV spectral range. The spectrometer is loaded with Kodak direct-exposure film (DEF)[19]. An array of five foil filter stacks, consisting of metal and plastic foils (Al, Ni, V, Ti, Cu and/or Kapton) with varying thicknesses (6 μm $- 100$ μm) is placed before each crystal, effectively dividing the x-ray film into five regions with varying levels of filtration, ensuring that at least one spectrum free of saturation effects is acquired on every shot. As the Kodak DEF film response, the filters spectral transmission, and the PET crystal reflectivity are well-known, the HENWAY spectra can be calibrated to determine absolute x-ray yield[5].

On the second campaign, the XCCS spectrometer was used with three different bent crystals (*channels*): Quartz, Beryl and PET. Their respective ranges are $6-17$ keV, $2.5 - 6$ keV and $6 - 14$ keV, with the respective average resolutions 600 eV, 30 eV and 100 eV. The detector is a charge injection device (CID) camera. Three slits placed between the target and the crystals provided ∼ 100 μm spatial resolution of the x-ray spectra along the target's cylinder axis. Note that XCCS was derived from the spectrometer described in Ref. 20, but its design is not identical.

HENWAY and XCCS provide high-resolution spectra, thus detailed information about the plasma temperature and charge distribution can be derived when compared to detailed atomic emission models.

D. Time-resolved x-ray spectrometers

Two time-resolved x-ray diode spectrometers (DANTE and DMX) were employed in these experiments. DANTE[21] measures x-ray power in up to 18 energy ranges (*channels*) spanning a wide range of energy (60 eV $- 15$ keV). The detectors are vacuum x-ray diodes with Al, Ni, or Cr cathodes and filtration depending on the frequency range to be detected. Time-resolved signals from the diodes are acquired using high-speed (5 GHz) digitizers. DANTE is absolutely calibrated using synchrotron radiation and ab-

solute x-ray yields can be determined from the waveforms of each channel.

DMX[22], like DANTE, is a time-resolved x-ray diode spectrometer that measures x-ray power across a wide energy range. DMX is sensitive to x rays from 50 eV to 20 keV, divided into 18 channels. The filtration and method of detection depend on energy. Emission in the low-energy channels $(< 1.5$ keV) is detected by coaxial diode detectors, placed behind a set of filters and mirrors that are designed to provide maximum hard x-ray rejection. Emission in the range $1.5 - 5.0$ keV is detected by a set of filtered coaxial diode detectors. Emission from $5 - 20$ keV is detected using a set of filtered photoconductive detectors. Like DANTE, DMX is absolutely calibrated using synchrotron radiation and absolute x-ray yields can be determined by integrating the time-resolved waveforms from each channel.

These two instruments provide calibrated time-resolved x-ray powers in several energy ranges, thus are the key diagnostics for measuring the laser-to-x-ray conversion efficiency.

E. X-ray imagers

An x-ray framing camera XRFC1[23] was employed in these experiments to observe target heating dynamics and verify beam pointing. It imaged the target's x-ray emission through an array of twelve pinholes onto a gated micro-channel plate detector. XRFC1 has a near-side-on view of the target (79° with respect to the target axis), and captures heat front propagation and plasma expansion along the target axis. Early-time images of the steel foil cavity targets also show localized heating and are used to verify beam pointing. XRFC1 is configured to produce three sequential exposures (each lasting 50 ps), beginning at t = 0.2 ns, 0.4 ns, 0.7 ns, and 1.0 ns (twelve exposures total). The camera is filtered with 15 μm-thick Ni foil to isolate Fe K-shell emission, and a 254 μm-thick Be foil to eliminate soft x-rays.

F. Backscattered light diagnostics

Laser backscatter measurements (stimulated Raman scattering, or SRS, and stimulated Brillouin scattering, or SBS) are performed using a suite of diagnostics on beams 25 and 30 (beam 25 only for the second campaign). Full Aperture Backscatter Stations (FABS)[24] measure the spectral time-history and total energy of light scattered directly back along the laser beam path. In each FABS instrument, laser backscatter is separated into two wavelength groups (400 to 700 nm for SRS, 351±1 nm for SBS), which are directed into separate optical streak cameras and calorimeters.

Near Backscatter Imaging (NBI) systems[24] capture the spatial distribution of light that is backscattered outside the volume of the laser beam. The NBI systems consist
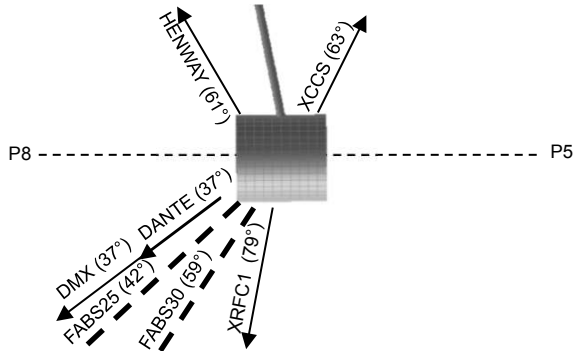
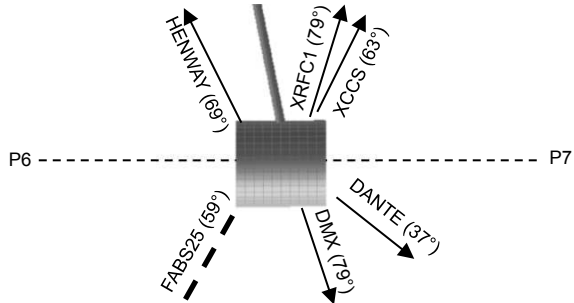FIG. 5. Diagnostics orientation in the first campaign.

FIG. 6. Diagnostics orientation in the second campaign.

of a white scatter plate that surrounds the beam entry port inside the target chamber, which is monitored by a CCD camera. The NBI data were used as backscatter calorimetry measurements.

G. Diagnostics orientation

The orientations of the diagnostic instruments described in the previous sections, with respect to the target axis, are detailed in Fig. 5 for the first campaign, and in Fig. 6 for the second campaign.

III. SIMULATIONS

Radiation-hydrodynamics simulations, which include atomic modeling for x-ray spectra estimation, have been carried out with the LASNEX code[12] for the different targets used during the experiments.

LASNEX is a 2D radiation-hydrodynamics computer code. The equations of motion are solved in a Lagrangian formulation, with the equation of state determined from the non-LTE rate equations. A ray-tracing algorithm simulates laser light propagation through matter, with inverse bremsstrahlung absorption on free electrons. The density of free electrons is determined from the ionization levels calculated in the incorporated super-configuration non-LTE atomic model[25]. Another key feature is that electron thermal conduction is treated in the Spitzer-
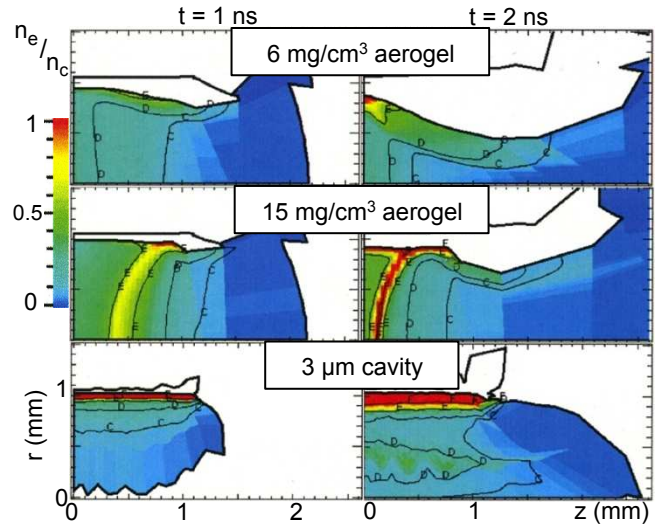

FIG. 7. (Color online) Electron density maps simulated by LASNEX, for different targets, at 1 and 2 ns. Only one quadrant of the simulation is drawn (z is the cylinder axis).
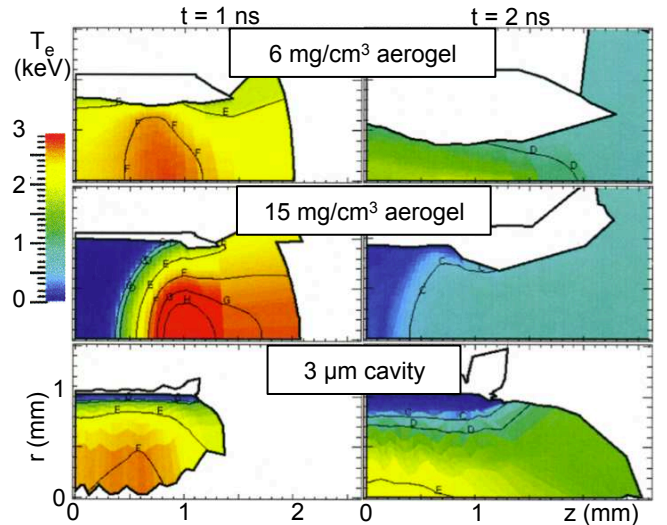

FIG. 8. (Color online) Electron temperature maps simulated by LASNEX, for different targets, at 1 and 2 ns.

Härm formulation[26] with a large flux limiter, $f = 0.2$, which provides for more non-local heat transport (more details of this model, its implementation and its benchmarking with experimental data from Ge-doped aerogels are given by Colvin et al.[27]). An in-line automatic re-zoning scheme was also devised, based on an equipotential method, that is specific for this particular geometry. In convergence studies, we verified that numerical diffusion introduced by the re-zoning scheme has negligible effect on the simulated x-ray emission.

The cylindrical-geometry simulations included a constant laser pulse during 1 ns, with 100 ps linear ramps at the beginning and at the end. A summary of the simulated electron density n_e and temperature T_e is given in Figs. 7 and 8 at 1 and 2 ns, for three different targets:

one 6 mg/cm^3 Fe aerogel, one 15 mg/cm^3 Fe aerogel, and one 3 μm-lined cavity.

The aerogel targets show different behaviors depending on their initial density. The 6 mg/cm^3 aerogels gradually heat up above 2.5 keV in the first 1 ns. The temperature is maximum where the laser interacts, but the low density of the foam allows the whole target to be heated up to an average electron temperature of 2 keV. Afterwards, the polyimide shell is hot enough to expand towards the cylinder axis. This provides foam compression, which thus stays hot longer than the laser pulse. The scenario is fairly different in the case of a 15 mg/cm^3 aerogel. Due to this higher density, the laser penetrates only in the first 300 μm of the target. This small volume expands outwards rapidly because its temperature peaks at 3.5 keV. Furthermore, the polyimide shell does not reach high temperatures so it does not expand and compress significantly the foam inside. As a consequence, the aerogel temperature drops very rapidly after the laser pulse is off.

To summarize the aerogels behaviors, two components are identified in favor of the low-density targets. First, the latter are heated volumetrically, thus potentially providing more x-ray emission. Second, the imploding shell compresses the foam and sustains a high T_e for a few more 100 ps, possibly leading to a longer x-ray emission.

Figs. 7 and 8 also illustrate the cavity targets simulation results. During 1 ns, the ablated plasma expands towards the cylinder axis, and the whole volume eventually reaches $T_e > 2$ keV, with a density very similar to the 6 mg/cm^3 aerogels. Afterwards, the plasma implodes on the cylinder axis, thus heats up again during an additional 1 ns. These observations imply a long x-ray emission from the cavity targets.

In order to compare the x-ray yields from these different simulations, we used the atomic model included into LASNEX to predict the x-ray flux between 5 and 9 keV (the Fe K-shell) as a function of time, and it is plotted in Fig. 9. As expected from the previous interpretation of Figs. 7 and 8, the high-density targets show a rapid increase of x-ray emission as the cylinder's faces heat up, and then a rapid decrease as they expand outwards. The low-density aerogels show slower variations in the x-ray flux because of the volumetric heating and the late axial compression explained above. Lastly, the cavity targets show a lower but longer x-ray flux, which corresponds well to the scenario described above (plasma gradually imploding on the cylinder axis). Overall, significantly different behaviors are predicted by the simulations, depending on the target type. However, the exact x-ray yield given by the simulations cannot be directly trusted because of the complexity of x-ray emission in this regime (keV temperatures and densities close to critical). Most importantly, the close tradeoff between volumetric heating and high electron density cannot be simulated well enough. For this reason, experimental measurements are essential and they are discussed in the next section.
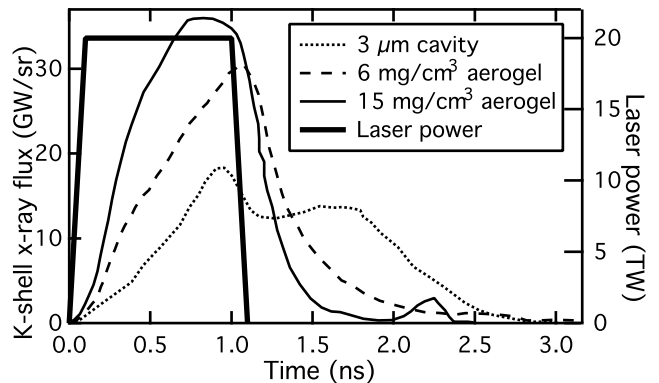

FIG. 9. K-shell x-ray flux *vs* time as simulated by LASNEX.

IV. DISCUSSION

A. Time-integrated spectra

Absolutely-calibrated K-shell emission spectra from the HENWAY diagnostic are shown in Figs. 10 and 11 for aerogel and steel cavity targets, respectively. H-like (Fe^{25+}), He-like (Fe^{24+}), and Li-like (Fe^{23+}) emission lines are observed and are labeled in Fig. 10. The spectra consist mainly of He-like lines, with smaller amounts of H-like and Li-like lines. X-ray emission is most intense for the lowest-density (6.5 mg/cm^3) aerogels and can be 50% weaker for the higher-density targets. In the case of the foil-lined cavity targets, the spectra are very similar, although additional lines from Cr, Mn and Ni are visible (see Fig. 11). The x-ray intensity shows only a weak dependence on foil thickness. Note that all these spectra agree well with those measured using the XCCS spectrometer.

Under the plasma conditions produced in these experiments ($T_e \sim 2$ keV, $n_e \sim 10^{21}$ cm^{-3} as predicted by LASNEX), line intensity ratios provide a convenient measure of electron temperature. Using the collisional-radiative code SCRAM[28], we determined that the line most affected by the electron temperature T_e is the Ly-α at 7.0 keV (the spectra are only very weakly dependent on electron density between $10^{20} - 10^{22}$ cm^{-3}). Thus, the ratio between the Ly-α and He-α lines is the most appropriate measurement in our case. The SCRAM simulations assume uniform electron density and temperature, and have been convoluted with a 20 eV full-width-at-half-maximum (FWHM) gaussian function representing HENWAY's spectral resolution. In order to get the right continuum background, they also account for the O and Cl elements of the aerogel in addition to Fe. A comparison between SCRAM simulated spectra and a corresponding HENWAY measured spectrum are given in Fig. 12 in the case of a 6 mg/cm^3 aerogel target. Recalling that the most important feature here is the Ly-α to He-α ratio, the best agreement is obtained for an electron temperature $T_e = 2000 \pm 200$ eV (the error bar corresponds to the

simulated spectrum being within the noise variation observed on the experimental spectrum). This agrees well with the simulation results from section III, as the corresponding average temperature was ~ 2 keV across the whole foam. Note that this conclusion does not apply to the higher density foams because their density and temperature profiles are not uniform enough.

X-ray emission from steel-cavity targets was predicted to be very similar to the 6 mg/cm^3 aerogels case, as their density and temperature profiles are alike. The Ly-α to He-α lines ratio was indeed found to be similar (Fig. 11),
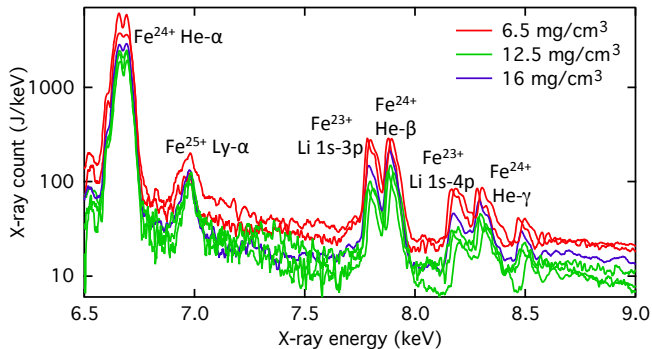

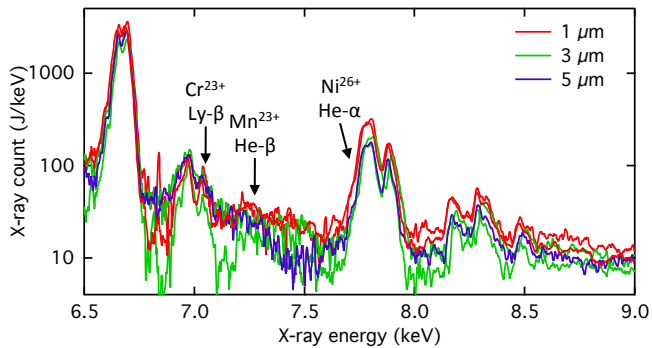FIG. 10. (Color online) HENWAY spectra from various aerogel targets.

FIG. 11. (Color online) HENWAY spectra from various steel cavity targets.
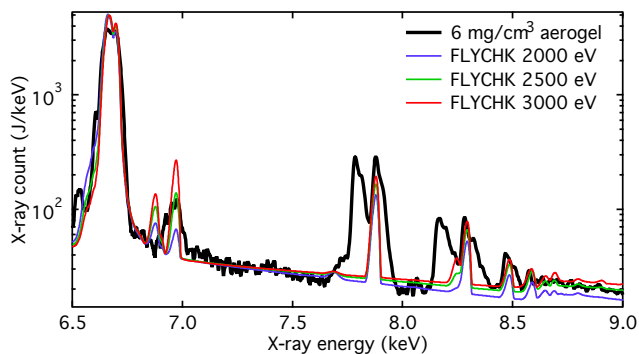

FIG. 12. (Color online) HENWAY vs SCRAM spectra comparison for a 6 mg/cm^3 aerogel. Note that the SCRAM simulated spectra have been normalized to the same maximum value.

validating again the 2 keV temperature reached by these targets (averaged in space and time). No significant effect of the steel thickness is observed in these spectra.

In summary, the high-resolution time-integrated spectra have confirmed the 2 keV average temperature predicted in the LASNEX simulations.

B. Time-resolved spectra

The recorded x-ray yields from each channel of the DANTE diagnostic were analyzed and the time-resolved spectrum was inferred for each shot using the technique described in Refs. 29 and 30. The spectral content in the Fe K-shell range was then extracted, and is plotted as a function of time in Figs. 13 and 14 for aerogels and cavity targets, respectively. The temporal x-ray emission is qualitatively different for these two types of targets.

As illustrated in Fig. 13, the aerogel targets tend to heat and cool monotonically. Apart from two 16 mg/cm^3 targets, there is a general trend for the low-density aerogels to emit x-rays longer in time. Most of the high-density aerogels show a sharp decrease after the peak, whereas almost all the low-density ones emit during an additional 1 or 2 ns. Note that both the 16 mg/cm^3 aerogels which do not conform to this trend did not completely fill the polyimide tubes in which they were cast; both were empty at one end, with polyimide tubes only $\sim 75\%$ full. As a result, the plasma produced on one face of the target likely continued to expand outward into the laser cones and continued to be heated by the laser. The third 16 mg/cm^3 aerogel was not defective, and conforms to the trend seen in the x-ray power from the lower density targets; these observations are consistent with the x-ray framing camera images discussed in the next sections.

These results are in qualitative agreement with the hydrodynamic simulations (Fig. 9). Indeed, the low-density aerogels were predicted to emit longer than the high-density ones, due to the volumetric heating and to the late recompression on the cylinder axis. The overall target dynamics are dominated by the softer radiation and hydrodynamic codes are expected to get the few-percent hard-x-ray output within a factor of two. To quantitatively assess the time-dependent hard-x-ray output more carefully, our strategy will be to use detailed atomic codes like SCRAM to post-process the simulation results.

Another important observation about the aerogels is the degree of scatter in the results for shots with the same densities. The targets were fabricated in several sets, and it appears that, within each set, the x-ray powers are similar. This suggests that the scatter observed in these results is mainly due to the batch-to-batch variation in the aerogel fabrication.

In contrast, the foil-lined cavity targets are fabricated more consistently and emit repeatable x-ray power from shot to shot (see Fig. 14), without any apparent influ-
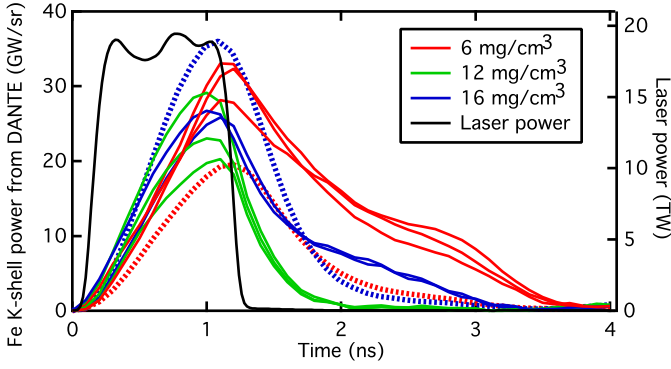
FIG. 13. (Color online) Fe K-shell x-ray power as a function of time for aerogel targets of different densities, as recorded by DANTE. Each line corresponds to a specific shot, the dotted lines being from the second campaign.
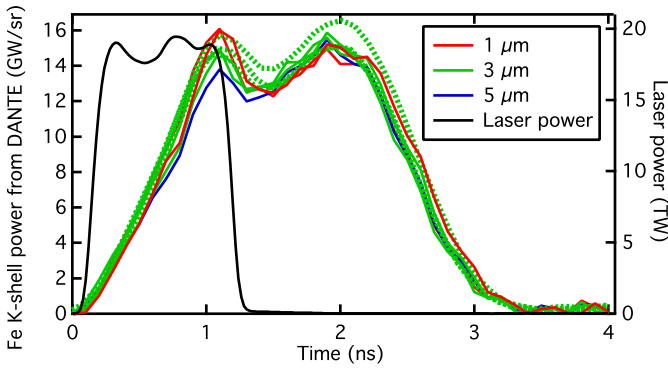

FIG. 14. (Color online) Fe K-shell x-ray power as a function of time for cavity targets of different steel thicknesses, as recorded by DANTE. Each line corresponds to a specific shot, the dotted lines being from the second campaign.

ence of the steel thickness. Furthermore, they appear to undergo two distinct phases of emission. As previously seen in the simulations, the targets are initially heated by the laser and emit K-shell x-rays. As the resulting plasma expands, it begins to cool, and K-shell emission begins to weaken. However, the plasma eventually fills the cavity and undergoes compression heating, resulting in a second emission maximum[10]. In fact, the x-ray flux from cavity targets are well reproduced by the simulations (see Fig. 9). The only difference is a constant ∼ 30% higher x-ray flux obtained experimentally, possibly explained again by the uncertainty in the x-ray emission simulation.

Note that all the discussion in this section is based on DANTE measurements, but the DMX diagnostic showed the same features.

C.   X-ray images

Time-resolved x-ray images from the framing camera are displayed in Fig. 15, showing images of K-shell emission for 6 mg/cm^3 and 12 mg/cm^3 aerogel targets. Four
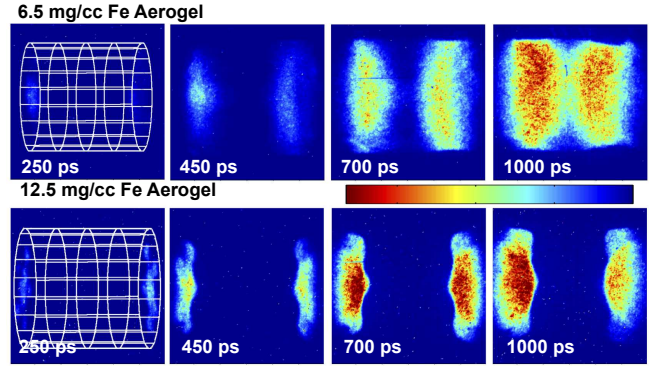

FIG. 15. (Color online) Fe K-shell emission images at different times, for two different densities of aerogel targets.
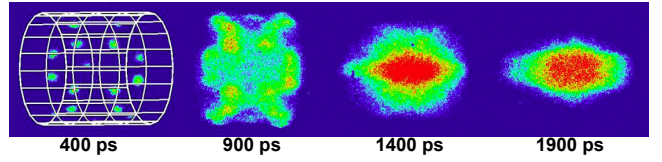

FIG. 16. (Color online) Fe K-shell emission images at different times, for a 3 μm cavity target. Note that the times are later than for the aerogel targets in Fig. 15.

images are taken up to 1 ns after the beginning of the laser pulse. The 6.5 mg/cm^3 target is quickly heated to the center, whereas the 12 mg/cm^3 target never gets heated deeper than a few 100 μm. This illustrates the qualitative difference in temporal heating dynamics for the low-density and higher-density targets: heat fronts propagate faster in the lower-density material, leading to the complete volumetric heating predicted in section III. As previously observed in section IV B, this induces a longer x-ray emission for the lower density targets.

In the case of cavity targets, the x-ray images in Fig. 16 show that the emission, initially coming from small spots on the cylinder wall, gets broader and eventually fills the whole cavity. After 1 ns, one can clearly see the hot plasma stagnate at the cylinder's center, providing a strong emission late in time. This matches very well both the spatial and temporal distributions of hot plasma predicted by the hydrodynamic simulations.

D.   X-ray yields

The integrated yields in the Fe K-shell range ($6.5 - 8.5$ keV), as measure by DANTE, DMX and HENWAY, are plotted in Fig. 17. For each point, the measurement uncertainty is always between ±4% and ±7%. The error bars are not displayed for clarity. Note that DANTE and DMX have identical views of the target only in the first campaign, but that the viewing factor has been accounted for in the yield calculation.

Both the low and high density aerogels (Fig. 17a)

demonstrate strong variation within 35 ± 15 J/sr, due to their challenging fabrication. No clear trend is visible in this figure, but the highest yields were obtained for low plasma densities. One would expect less yield due to the lower number of Fe atoms per unit volume. However, thanks to volumetric heating of these low-density aerogels, a larger volume is able to emit K-shell x-rays. This can explain why we observe an increasing x-ray yield for low-densities instead of a decreasing yield.

In comparison, the cavities (Fig. 17b), due to their easier fabrication process, show a reproducible yield of 30 ± 5 J/sr independent of the steel thickness. Note that the HENWAY yields are somewhat more scattered because of background issues on several shots.

The total yields (0 to 20 keV) measured by DANTE and DMX are plotted in Fig. 18. There is no clear trend as a function of either aerogel density or steel thickness. The cavity targets appear to emit more than aerogels (~ 1100 $vs \sim 800$ J/sr) in this full x-ray range, whereas we found above that they emitted slightly less in the Fe K-shell range.

In terms of laser-to-x-ray conversion efficiency, the results are summarized in Table I. As explained before, the x-ray model included in the simulations may not be complete enough to provide exact predictions. In fact, it appears to predict well the high-density aerogels, but under-estimates the yields from the other types of targets.

	Fe K-shell CE	Total CE
Low-density aerogel	$1.8 - 3\%$	$50 - 60\%$
	(1.8 %)	(42 %)
High-density aerogel	$1.2 - 2\%$	$35 - 45\%$
	(2.1 %)	(44 %)
Steel-lined cavity	$1.6 - 2.2\%$	$60 - 75\%$
	(1.5%)	(45 %)

Table I. Experimental laser-to-x-ray conversion efficiencies (CE) in the Fe K-shell range ($6.5 - 8.5$ keV) and the full x-ray range. Results from LASNEX simulations are provided in parentheses.

E. Backscattered light measurements

The backscatter calorimetry measurements show that there is always 2 to 5 times more reflected light from SBS than SRS, and the total amount depends on the target type and on the laser incident angle (see Fig. 3). For aerogels, there is $1.4 - 2.6\%$ scattered light in cone 2 and $2 - 6\%$ in cone 3. For cavities, the opposite trend was measured: $3 - 4\%$ in cone 2 and $\sim 1\%$ in cone 3. This qualitatively agrees with the target shapes. Indeed, cone 3 is at shallow incidence to the face of the aerogels, but is closer to the normal of the cavity walls, which is why cone 3 scatters less in the case of cavities (in other terms, there is a 90° rotation of the surface between these
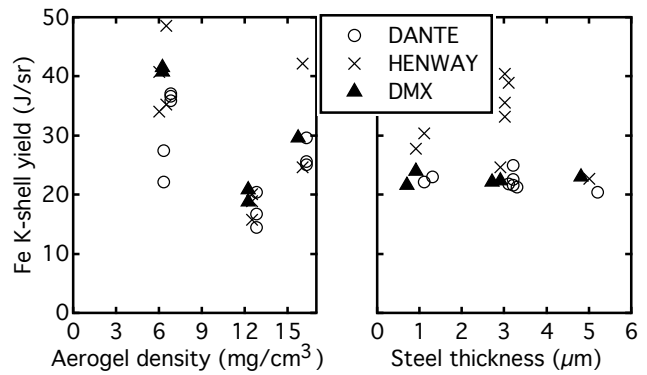

FIG. 17. Fe K-shell yields from (a) aerogel and (b) cavity targets, as measured by DANTE, HENWAY and DMX.
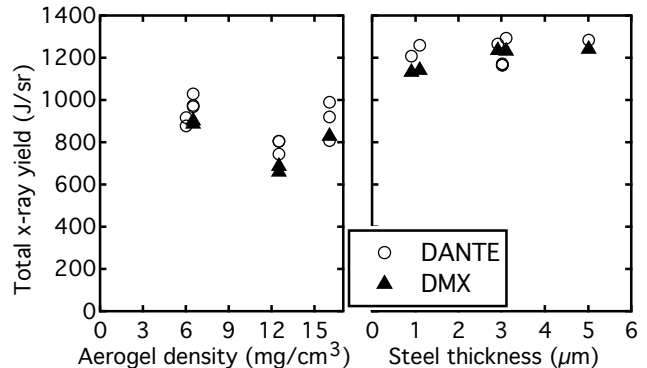

FIG. 18. Total x-ray yields from (a) aerogel and (b) cavity targets, as measured by DANTE and DMX.

two cases). Overall, accounting for all beams, all targets showed $< 5\%$ reflectivity, and typiclly below 2.5%.

The SRS and SBS data were also available in the form of time-resolved (streaked) spectra, which can provide useful information about the plasma state close to the laser interaction region. Let us begin with SRS spectra which, as illustrated in Fig. 19, strongly depend on the type of target used. In the case of 12 mg/cm^3 aerogels (Fig. 19b), a fairly constant 1 ns-long SRS reflectivity is observed, with a typical redshift of 300 nm. This suggests that the plasma conditions in the interaction region do not vary significantly during the first nanosecond. Furthermore, this redshift is associated with an electron density[31] $n_e/n_c \sim 0.1$, which is the value predicted by LASNEX at the cylinder faces. Now, two differences are observed for the low-density aerogels (Fig. 19a). First, the SRS intensity decreases with time: the laser heats deeper parts of the targets, thus less scattered light can reach the SRS detector. This feature confirms once again the volumetric heating of 6 mg/cm^3 aerogels. Second, the redshift decreases with time, indicating that n_e, at the cylinder's faces, decreases. More precisely, as the heating region goes deeper into the target, the faces begin to cool down early (LASNEX also confirmed this effect).

The SRS signals of cavity targets (see Fig. 19c) present a much stronger time dependence: at the beginning of

the laser pulse, no signal is collected. Indeed, the sharp cavity walls do not provide enough plasma gradients for the SRS instability to grow. It actually arises only after 0.5 ns, with a redshift corresponding to $n_e/n_c \sim 0.1$. This signal was attributed, in previous experiments[8], to plasma expansion clipping the laser path, generated by the opposite lasers. This induces scattering later in time, which explains the SRS spectra we obtained (the LASNEX simulations presented in III showed that, after 0.5 ns, enough plasma has expanded to clip part of the laser paths).

SBS streaked spectra are plotted for various targets in Fig. 20. Their interpretation is more challenging as the wavelength shift depends on both the plasma temperature (the redshift depends on T_e) and its drift velocity (through the Doppler effect). For aerogels, more redshift is observed, which confirms once again that they do not undergo rapid expansion during the first nanosecond, but instead heat up rapidly. The maximum redshift is associated to a temperature of $3 - 3.5$ keV[31]. This is in good agreement with the LASNEX simulations showing that targets do not heat up significantly above 3.5 keV. Furthermore, the high-density aerogels scatter at all wavelengths between 351 and 352 nm, which corresponds to their strong temperature gradients, whereas the 6 mg/cm^3 aerogels show a thin spectrum around 351.8 nm, which proves they are fairly uniform in temperature (2 to 3 keV). Lastly, the time-dependence of the

FIG. 19. (Color online) Typical time-resolved SRS spectra from the FABS instrument for (a) 6 mg/cm^3 aerogel, (b) 12 mg/cm^3 aerogel and (c) 1 μm-thick steel cavity. The line at 527 nm is a fiducial representing the laser duration.

FIG. 20. (Color online) Typical time-resolved SBS spectra from the FABS instrument for (a) 6 mg/cm^3 aerogel, (b) 12 mg/cm^3 aerogel and (c) 1 μm-thick steel cavity. The line at 351 nm is a fiducial representing the laser duration.

SBS signal for aerogels is fairly similar to the SRS one: short for low-density aerogels, and longer for high-density aerogels. All these observations from SBS support once again the volumetric heating process (for the low-density targets), as it allows laser-plasma interaction to happen deeper in the plasma.

In contrast, the steel cavities mostly exhibit blueshift, which indicates that their expansion dominates the SBS signal. Their associated plasma drift velocity rises up to ~ 0.5 mm/ns during the first 0.3 ns (typically confirmed by LASNEX).

Note that the SRS/SBS data analysis is kept at a qualitative level in this paper as our goal is not to investigate the laser-plasma interaction, but to report on x-ray production and on the underlying hydrodynamic behavior. Scattered-light simulations related to this kind of experiment will be carried out for future publication.

V. CONCLUSIONS

Overall, the different diagnostics used in these experiments confirmed the simulated hydrodynamic behaviour of the Fe-based targets. As a consequence, the following scenarios can be described. In the case of aerogels with a density above 10 mg/cm^3, the laser-induced heating stays localized at the target surfaces. These surfaces emit a high x-ray yield per unit volume, but it rapidly drops due to plasma expansion. For aerogel densities below 10 mg/cm^3, the plasma is heated much deeper. This volumetric heating provides a stronger total x-ray emission, the laser energy being overall more efficiently converted to K-shell x rays. This situation induces an ablation of the polyimide tube that then compresses the plasma inside, providing some more x-ray flux at later times. By going to lower aerogel densities, it is then possible to increase both the duration of the K-shell x-ray emission and its yield. These two features are fundamental parameters for high-energy x-ray sources, thus low-density aerogels are a promising tool in this research. As observed for the iron aerogels of the present work, their fabrication is still challenging, and a lot of shot-to-shot variation can be expected. Eventually, manufacturing such targets will be better controlled, possibly providing even higher amount of high-Z material, and higher fluxes.

In contrast, the other type of targets presented in this paper, Fe-lined cavities, exhibit a very good shot-to-shot reproducibility. Indeed, their fabrication is easier than aerogels. The duration of the x-ray emission (~ 2 ns) is also one of their advantages as it happens in two phases: laser heating on the cavity walls, then compression heating of the plasma on the cylinder axis. However, the yield cannot be adjusted by changing the steel thickness. For now, these targets are limited in terms of the hard-x-ray yield they can achieve. Furthermore, their higher soft-x-ray yield (< 2 keV) can be detrimental to some applications.

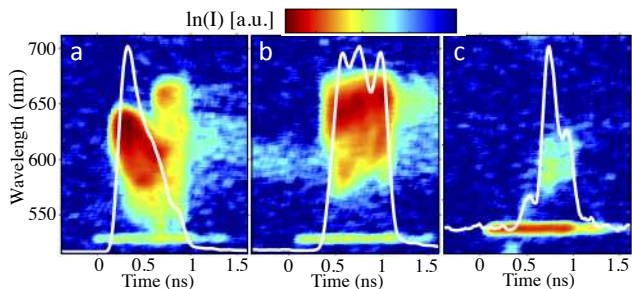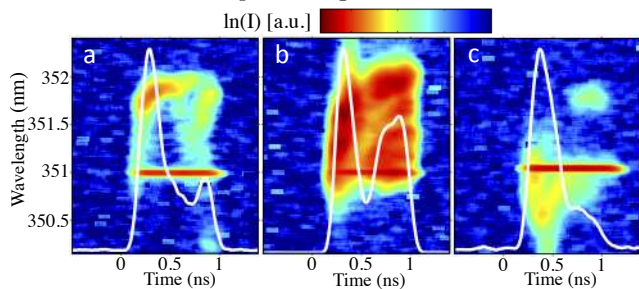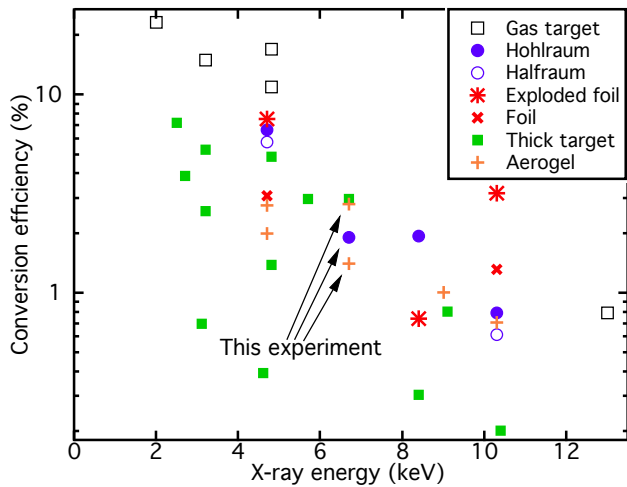In summary, all these results complete previous exper-

FIG. 21. (Color online) Laser-to-x-ray conversion efficiencies obtained in various experiments, as reported in Ref. 10. Arrows indicate the results from the present paper.

iments on the same subject by introducing a new element in the list of potential candidates for bright hard-x-ray sources (see Ref. 10 and references within). Our Fe targets provide ~ 7 keV radiation, a good intermediate value between the more common Ti and Ge targets, at ~ 5 keV and ~ 10 keV, respectively. As seen in Fig. 21, our measured conversion efficiencies fit well in the trend obtained from previous experiments. It confirms that Fe-based targets are good candidates for bright ns-scale x-ray sources. Aerogels and cavities seem to be equally efficient in the Fe K-shell range, and better results could still be achieved with even lower density aerogels. Metallic aerogel target development is thus an important part of this research, as is becomes extremely challenging to control lower densities. Future experiments will aim towards such low-density targets, with a high concentration of metallic atoms, in order to increase the x-ray yield.

ACKNOWLEDGMENTS

REFERENCES

[1] J. Workman and G. A. Kyrala, Review of Scientific Instruments **72**, 678 (2001).

[2] F. Girard, J. P. Jadaud, M. Naudy, B. Villette, D. Babonneau, M. Primout, M. C. Miller, R. L. Kauffman, L. J. Suter, J. Grun, and J. Davis, Physics of Plasmas **12**, 092705 (2005).

[3] D. Babonneau, M. Primout, F. Girard, J. P. Jadaud, M. Naudy, B. Villette, S. Depierreux, C. Blancard, G. Faussurier, K. B. Fournier, L. Suter, R. Kauffman, S. Glenzer, M. C. Miller, J. Grün, and J. Davis, Physics of Plasmas **15**, 092702 (2008).

[4] K. B. Fournier, C. Constantin, J. Poco, M. C. Miller, C. A. Back, L. J. Suter, J. Satcher, J. Davis, and J. Grun, Physical Review Letters **92**, 165005 (2004).

[5] K. B. Fournier, J. H. Satcher, M. J. May, J. F. Poco, C. M. Sorce, J. D. Colvin, S. B. Hansen, S. A. MacLaren, S. J. Moon, J. F. Davis, F. Girard, B. Villette, M. Primout, D. Babonneau, C. A. Coverdale, and D. E. Beutler, Physics of Plasmas **16**, 052703 (2009).

[6] M. Tanabe, H. Nishimura, S. Fujioka, K. Nagai, N. Yamamoto, Z. Gu, C. Pan, F. Girard, M. Primout, B. Villette, D. Brebion, K. B. Fournier, A. Fujishima, and K. Mima, Applied Physics Letters **93**, 051505 (2008).

[7] K. Fournier, C. Constantin, C. Back, L. Suter, H. Chung, M. Miller, D. Froula, G. Gregori, S. Glenzer, E. Dewald, and O. Landen, Journal of Quantitative Spectroscopy and Radiative Transfer **99**, 186 (2006).

[8] K. B. Fournier, M. J. May, J. D. Colvin, J. O. Kane, M. Schneider, E. Dewald, C. A. Thomas, S. Compton, R. E. Marrs, J. Moody, E. Bond, P. Michel, J. H. Fisher, C. D. Newlander, and J. F. Davis, Physics of Plasmas **17**, 082701 (2010).

[9] M. Primout, L. Jacquet, D. Babonneau, F. Girard, B. Villette, J.-P. Jadaud, M. Naudy, P. Stemmler, and J. L. Ulmer, Journal of Physics: Conference Series **112**, 042051 (2008).

[10] F. Girard, M. Primout, B. Villette, P. Stemmler, L. Jacquet, D. Babonneau, and K. B. Fournier, Physics of Plasmas **16**, 052704 (2009); Physics of Plasmas **18**, 079901 (2011).

[11] C. A. Back, J. Grun, C. Decker, L. J. Suter, J. Davis, O. L. Landen, R. Wallace, W. W. Hsing, J. M. Laming, U. Feldman, M. C. Miller, and C. Wuest, Physical Review Letters **87**, 275003 (2001).

[12] J. A. Harte, W. E. Alley, D. S. Bailey, J. L. Eddleman, and G. B. Zimmerman, ICF Quarterly Report, July-September 1996, Volume 6, Number 4, Lawrence Livermore National Laboratory, document no. UCRL-LR-105821-96-4.

[13] G. H. Miller, E. I. Moses, and C. R. Wuest, Optical Engineering **43**, 2841 (2004).

[14] A. E. Gash, J. H. Satcher, and R. L. Simpson, Chem. Mater. **15**, 3268 (2003).

[15] J. M. Soures, R. L. McCrory, C. P. Verdon, A. Babushkin, R. E. Bahr, T. R. Boehly, R. Boni, D. K. Bradley, D. L. Brown, R. S. Craxton, J. A. Delettrez, W. R. Donaldson, R. Epstein, P. A. Jaanimagi, S. D. Jacobs, K. Kearney, R. L. Keck, J. H. Kelly, T. J. Kessler, R. L. Kremens, J. P. Knauer, S. A. Kumpan, S. A. Letzring, D. J. Lonobile, S. J. Loucks, L. D. Lund, F. J. Marshall, P. W. McKenty, D. D. Meyerhofer, S. F. B. Morse, A. Okishev, S. Papernov, G. Pien, W. Seka, R. Short, M. J. Shoup, M. Skeldon, S. Skupsky, A. W. Schmid, J. D. Smith, S. Swales, M. Wittman, and B. Yaakobi, Physics of Plasmas **3**, 2108 (1996).

[16] S. P. Regan, T. C. Sangster, D. D. Meyerhofer, W. Seka, R. Epstein, S. J. Loucks, R. L. McCrory, C. Stoeckl, V. Y. Glebov, O. S. Jones, D. A. Callahan, P. A. Amendt, N. B. Meezan, L. J. Suter, M. D. Rosen, O. L. Landen, E. L. Dewald, S. H. Glenzer, C. Sorce, S. Dixit, R. E. Turner, and B. J. MacGowan, Journal of Physics: Conference Series **112**, 022077 (2008).

[17] National Laser User Facility User's Guide (2007).

[18] L. N. Koppel and J. D. Eckels, "National technical information service document No. UCRL-79781," (1977).

[19] C. A. Back, J. Davis, J. Grun, L. J. Suter, O. L. Landen, W. W. Hsing, and M. C. Miller, Physics of Plasmas **10**, 2047 (2003).

[20] C. Reverdin, A. S. Morlens, B. Angelier, J. L. Bourgade, J. Y. Boutin, M. Briat, G. Charles, A. Duval, A. Estadieu, C. Cholet, D. Gontier, D. Husson, H. P. Jacquet, J. P. LeBreton, G. Lidove, B. Marchet, R. Marmoret, R. Maroni, P. Millier, J. Raimbourg, C. Remond, R. Rosch, G. Soullié, P. Stemmler, P. Troussel, J. L. Ulmer, B. Villette, and R. Wrobel, Review of Scientific Instruments **75**, 3730 (2004).

[21] H. N. Kornblum, R. L. Kauffman, and J. A. Smith, Review of Scientific Instruments **57**, 2179 (1986).

[22] J. L. Bourgade, B. Villette, J. L. Bocher, J. Y. Boutin, S. Chiche, N. Dague, D. Gontier, J. P. Jadaud, B. Savale, R. Wrobel, and

R. E. Turner, Review of Scientific Instruments **72**, 1173 (2001).

[23] D. K. Bradley, P. M. Bell, J. D. Kilkenny, R. Hanks, O. Landen, P. A. Jaanimagi, P. W. McKenty, and C. P. Verdon, Review of Scientific Instruments **63**, 4813 (1992).

[24] P. Neumayer, C. Sorce, D. H. Froula, L. Divol, V. Rekow, K. Loughman, R. Knight, S. H. Glenzer, R. Bahr, and W. Seka, Review of Scientific Instruments **79**, 10F548 (2008).

[25] H. Scott and S. Hansen, High Energy Density Physics **6**, 39 (2010).

[26] L. Spitzer and R. Härm, Physical Review **89**, 977 (1953).

[27] J. D. Colvin, K. B. Fournier, M. J. May, and H. A. Scott, Physics of Plasmas **17**, 073111 (2010).

[28] S. Hansen, J. Bauche, C. Bauche-Arnoult, and M. Gu, High Energy Density Physics **3**, 109 (2007).

[29] R. L. Kauffman, H. N. Kornblum, D. W. Phillion, C. B. Darrow, B. F. Lasinski, L. J. Suter, A. R. Theissen, R. J. Wallace, and F. Ze, Review of Scientific Instruments **66**, 678 (1995).

[30] A. Seifter and G. A. Kyrala, Review of Scientific Instruments **79**, 10F323 (2008).

[31] W. L. Kruer, *The physics of laser plasma interactions* (Westview Press, 2003).